# Calibration of an expeditious terramechanics model using a higher-fidelity model, Bayesian inference, and a virtual bevameter test

**Wei Hu**
Department of Mechanical Engineering
University of Wisconsin-Madison
Madison, WI 53706, USA
whu59@wisc.edu

**Pei Li**
Department of Mechanical Engineering
University of Wisconsin-Madison
Madison, WI 53706, USA
lipeibit@gmail.com

**Huzaifa Mustafa Unjhawala**
Department of Mechanical Engineering
University of Wisconsin-Madison
Madison, WI 53706, USA
unjhawala@wisc.edu

**Radu Serban**
Department of Mechanical Engineering
University of Wisconsin-Madison
Madison, WI 53706, USA
serban@wisc.edu

**Dan Negrut***
Department of Mechanical Engineering
University of Wisconsin-Madison
Madison, WI 53706, USA
negrut@wisc.edu

## Abstract

The soil contact model (SCM) is widely used in practice for off-road wheeled vehicle mobility studies when simulation speed is important and highly accurate results are not a main concern. In practice, the SCM parameters are obtained via a bevameter test, which requires a complex apparatus and experimental procedure. Here, we advance the idea of running a virtual bevameter test using a high-fidelity terramechanics simulation. The latter employs the "continuous representation model" (CRM), which regards the deformable terrain as an elasto-plastic continuum that is spatially discretized using the smoothed particle hydrodynamics (SPH) method. The approach embraced is as follows: a virtual bevameter test is run in simulation using CRM terrain to generate "ground truth" data; in a Bayesian framework, this data is subsequently used to calibrate the SCM terrain. We show that (*i*) the resulting SCM terrain, while leading to fast terramechanics simulations, serves as a good proxy for the more complex CRM terrain; and (*ii*) the SCM-over-CRM simulation speedup is roughly one order of magnitude. These conclusions are reached in conjunction with two tests: a single wheel test, and a full rover simulation. The SCM and CRM simulations are run in an open-source software called Chrono. The calibration is performed using PyMC, which is a Python package that interactively communicates with Chrono to calibrate SCM. The models and scripts used in this contribution are available as open source for unfettered use and distribution in a public repository.

Keywords: Continuous representation model; Smoothed particle hydrodynamics (SPH); Soil contact model; Calibration; Bayesian inference; Terramechanics; Virtual bevameter test

*Corresponding author

# 1 Introduction

The golden standard in many terramechanics applications is the discrete element method (DEM) (Cundall and Strack, 1979; Iwashita and Oda, 1999; Jensen et al., 1999). Since the DEM approach treats each individual grain in the deformable terrain as a discrete body engaged in frictional contact with its neighbors, it delivers a high fidelity numerical solution. For this reason, it has been used in many engineering terramechanics applications that involved complex mechanical systems, e.g., (Johnson et al., 2015; Ucgul et al., 2015; Zhao and Zang, 2017; Recuero et al., 2017; Negrut and Mazhar, 2017). However, the computational cost of a fully resolved DEM simulation is typically prohibitively high since the method resolves the dynamics of each individual grain. Fortunately, highly accurate terramechanics is not always necessary. For instance, if the goal is to test the path planning module of an autonomy stack, or a state estimation algorithm, resolving the terrain with high fidelity is not mandatory. As such, over the last decade there has been increased interest in homogenizing the terrain and employing a continuum representation method (CRM) in an attempt to reduce simulation times. In CRM, the continuum representation is spatially discretized using either a finite element method (FEM) approach (Chauchat and Médale, 2014; Ionescu et al., 2015); or a particle-based solution, see, for instance, the material point method (Sulsky et al., 1994; Bardenhagen et al., 2000; Soga et al., 2016; Baumgarten and Kamrin, 2019), and the smoothed particle hydrodynamics (SPH) method (Bui et al., 2008; Chen and Qiu, 2012; Nguyen et al., 2017; Hurley and Andrade, 2017; Hu et al., 2021a; Hu et al., 2022b). Going from a discrete to a continuum representation of the terrain leads to a significant reduction in the degree-of-freedom (DOF) count, which in our experience leads to a one to two order of magnitude reduction in simulation times (Chen et al., 2020; Xu et al., 2019; Hu et al., 2021a). This has led, for instance, to mobility simulations of the VIPER Moon and Curiosity Mars rovers in different testing scenarios (uphill, downhill, and tilted deformable terrain) (Hu et al., 2021b; Hu et al., 2022b). The real-time factor (RTF) for CRM can be as low as 30-150, where the RTF indicates how many seconds of run time it takes to simulate one second of vehicle locomotion over a deformable terrain. By comparison, DEM terramechanics simulations display RTFs in the range 3000 to 15 000 (Recuero et al., 2017).

Although CRM has achieved a significant performance improvement when compared with the DEM approach, it still remains too costly for human-in-the-loop simulation (Chiang et al., 2010; DeDonato et al., 2015), or when one needs to run multiple simulations to test in the loop, for instance, new autonomy stack algorithms, e.g., state estimators, path planners, control policies. Should simulation speed be the prevailing concern, the semi-empirical soil contact model (SCM) (Krenn and Hirzinger, 2009; Krenn and Gibbesch, 2011) that draws on the Bekker-Wong (Bekker, 1956; Wong, 2001) and Janosi-Hanamoto (Janosi and Hanamoto, 1961) models is a more suitable candidate since it has an RTF close to 1. The SCM model captures satisfactorily the wheel-soil interactions in cases when slip is low, the sinkage is small, and the wheel geometry is close to that of a cylinder (Smith et al., 2014; Meirion-Griffith and Spenko, 2011). Unlike DEM or CRM, which are physics-based and draw on parameters that have engineering meaning, e.g., bulk density, friction angle, Young's modulus, SCM is an empirical method whose parameters cannot be directly obtained from physical quantities associated with the terrain. In practice, the SCM parameters are obtained using a bevameter test rig (Apfelbeck et al., 2011; Edwards et al., 2017; Mason et al., 2020), which is used to perform a plate sinkage test and an annulus shear test. The former is performed to calibrate the parameters associated with the Bekker-Wong formula; the latter test is performed to calibrate the Janosi-Hanamoto parameters. Note that once the terrain proprieties change, the tests should be performed yet again to get a new set of SCM parameters. This is time consuming and expensive if not outright impractical.

This contribution proposes an alternate strategy for obtaining SCM parameters. Instead of carrying expensive bevameter tests, one leverages the fact that CRM is a physics-based method. Specifically, using known physical properties of the terrain, we use a virtual bevameter in conjunction with a CRM terrain to carry out the sinkage and annulus shear tests *in simulation*. The virtual bevameter is set up in a multibody dynamics code (Tasora et al., 2016), and the CRM solution is as described in (Hu et al., 2021a). Since the CRM approach is more accurate than the SCM approach, the "experimental" data produced by the virtual bevameter is used in lieu of the real experimental data to calibrate the SCM parameters. For calibration, we employ a Bayesian inference framework (Gelman et al., 1995; Robert, 2015) and a third-party package

called PyMC (Salvatier et al., 2016). A posterior distribution is obtained for the likelihood of the SCM parameters. Herein, we chose the maximum likelihood set of SCM parameters, and show that this choice leads to an SCM model that serves as a good proxy for the CRM terrain at a fraction of the cost.

This contribution is organized as follows. Section 2 outlines: (*i*) the SCM and CRM approaches for modeling deformable terrain; and (*ii*) the Bayesian inference framework employed to calibrate the SCM parameters via PyMC. In Section 3, a virtual bevameter rig is introduced to explain how the "experimental" data is generated in conjunction with the CRM model. In Section 4, both single wheel and VIPER rover simulations are performed using the SCM model. Therein, the SCM results are compared with the results obtained when the single wheel and rover simulations employ the CRM terrain used in the SCM calibration. Section 5 summarizes concluding remarks and directions of future work. All simulations carried out in this contribution draw on models available in a public repository for reproducibility studies, as well as unfettered use and distribution (Hu et al., 2022a).

# 2 Prerequisites

The proposed calibration methodology, which uses a virtual bevameter test, relies on two terramechanics models – SCM and CRM, and draws on a Bayesian calibration framework implemented in a software package called PyMC. This section covers these prerequisites – SCM, CRM, Bayesian inference, and PyMC-anchored framework – before detailing the overall calibration methodology in Section 3.

## 2.1 Overview of the SCM method

The SCM approach embraced draws on work reported in (Krenn and Hirzinger, 2009; Krenn and Gibbesch, 2011). It is a generalization of the Bekker formula, which relates the normal pressure $p$ to the sinkage $z$ for a wheel of width $b$ using a semi-empirical, experiment-based curve fitting with parameters $K_c$, $K_\phi$, and $n$ (Bekker, 1956):

$$p = (\frac{K_c}{b} + K_\phi) z^n \, . \tag{1}$$

SCM generalizes this formula to arbitrary collision shapes and terrain topologies. The overlap between collision shapes and terrain is found by casting rays from multiple terrain nodes and doing ray intersection tests with all collision shapes present in the simulation. Disjoint contact patches are identified and Eq. (1) is subsequently applied for each one, using an approximation $b \approx \frac{1}{2}\frac{P_{\text{patch}}}{A_{\text{patch}}}$ based on the contact patch area $A_{\text{patch}}$, and perimeter $P_{\text{patch}}$. The Bekker-Wong formula is combined with the Janosi-Hanamoto formula, the latter used to evaluate the shear stress between the wheel and terrain (Janosi and Hanamoto, 1961):

$$\tau = \tau_{\max}(1 - e^{-J_s/K_s}) \, , \tag{2}$$

where

$$\tau_{\max} = c + p \tan\varphi \, , \tag{3}$$

and $J_s$ is the accumulated shear displacement, $c$ is the cohesion coefficient, $\varphi$ the internal friction angle, and $K_s$ the so-called Janosi parameter. Together, Eqs. (1) and (2) can be used to apply normal and tangential contact forces on the impactor object, all while keeping track of the soil deformation (which is assumed to be only along the SCM normal direction). The Chrono implementation of SCM (Tasora et al., 2019; Serban et al., 2022) provides real-time vehicle-terrain simulation capabilities for deformable terrains in the presence of low to medium wheel slip ratios. For more details on the core principles of SCM, the reader is directed to (Krenn and Hirzinger, 2009; Krenn and Gibbesch, 2011; Tasora et al., 2019).

### 2.2 Overview of the CRM method

For CRM, we employ a homogenization of the granular material and use an elasto-plastic continuum model to capture the dynamics of the deformable terrain (Dunatunga and Kamrin, 2015). Herein, the CRM solution is obtained using the SPH method, which is a Lagrangian particle-based solution that requires no background grid (Lucy, 1977; Gingold and Monaghan, 1977). The state information is advected with the SPH particles, and the dynamics equations are enforced at the location of the SPH particles. The particles move based on the interactions among neighbor particles and the external forces, e.g. gravity. The SPH method has proven effective and efficient in simulating granular material problems with large deformation (Nguyen et al., 2017; Hurley and Andrade, 2017; Hu et al., 2021a; Hu et al., 2022b).

In CRM, the problem unknowns, i.e., field velocity vector $\mathbf{u}$ and the Cauchy stress tensor $\boldsymbol{\sigma}$, enter the mass and momentum balance equations as

$$\begin{cases} \frac{\mathrm{d}\mathbf{u}}{\mathrm{d}t} = \frac{\nabla\boldsymbol{\sigma}}{\rho} + \mathbf{f}_b \\ \frac{\mathrm{d}\rho}{\mathrm{d}t} = -\rho\nabla\cdot\mathbf{u} \end{cases} , \tag{4}$$

where $\rho$ is the density of the deformable terrain, and $\mathbf{f}_b$ represents external forces, e.g., the gravity force. The total stress tensor $\boldsymbol{\sigma} \in \mathbb{R}^{3\times3}$ is split in two components expressed as $\boldsymbol{\sigma} \equiv -p\mathbf{I} + \boldsymbol{\tau}$, where $\boldsymbol{\tau}$ is the deviatoric component of the total stress tensor and $p$ is the pressure which can be calculated from the trace of the total stress tensor as $p = -\frac{1}{3}\mathrm{tr}(\boldsymbol{\sigma}) = -\frac{1}{3}(\sigma_{xx} + \sigma_{yy} + \sigma_{zz})$.

For closure, a stress rate tensor formula is employed. We use Hooke's law as well as the work described in (Monaghan, 2000; Gray et al., 2001; Yue et al., 2015; Dunatunga and Kamrin, 2015) to express the objective total stress rate tensor as

$$\frac{\mathrm{d}\boldsymbol{\sigma}}{\mathrm{d}t} = \dot{\boldsymbol{\phi}}\cdot\boldsymbol{\sigma} - \boldsymbol{\sigma}\cdot\dot{\boldsymbol{\phi}} + 2G[\dot{\boldsymbol{\varepsilon}} - \frac{1}{3}\mathrm{tr}(\dot{\boldsymbol{\varepsilon}})\mathbf{I}] + \frac{1}{3}K\mathrm{tr}(\dot{\boldsymbol{\varepsilon}})\mathbf{I}\,. \tag{5}$$

In Eq. (5), when the material is not subject to plastic flow, the elastic strain rate tensor $\dot{\boldsymbol{\varepsilon}}$ of the granular material is defined as $\dot{\boldsymbol{\varepsilon}} = \frac{1}{2}[\nabla\mathbf{u} + (\nabla\mathbf{u})^T]$; the rotation rate tensor is expressed as $\dot{\boldsymbol{\phi}} = \frac{1}{2}[\nabla\mathbf{u} - (\nabla\mathbf{u})^T]$. Herein, $G$ and $K$ denote the shear modulus and bulk modulus of the granular material-like deformable terrain, respectively, and $\mathbf{I}$ is the identity matrix. It is noted that the expression of the elastic strain rate tensor given above only works in cases without a plastic flow. Once the granular material starts to flow, the elastic strain rate tensor is defined as

$$\dot{\boldsymbol{\varepsilon}} = \frac{1}{2}[\nabla\mathbf{u} + (\nabla\mathbf{u})^T] - \frac{\dot{\lambda}}{\sqrt{2}}\frac{\boldsymbol{\tau}}{\bar{\tau}}\,, \tag{6}$$

in which the second term on the right-hand side comes from the contribution of the plastic flow of the continuum representation of the granular material. Therein, $\dot{\lambda}$ and $\bar{\tau}$ are the plastic strain rate and equivalent shear stress, respectively (Dunatunga and Kamrin, 2015).

We use the SPH method to spatially discretize the mass and momentum balance equations in Eq. (4) and the expression of total stress rate tensor in Eq. (5). In SPH, the simulation domain (including the deformable granular material terrain, solid bodies, and wall boundaries) is discretized using SPH and BCE particles. The former are used in conjunction with the deformable granular material terrain, with which they advect. The motion of the SPH particles is obtained by solving the governing equations, see Eqs. (4) and (5). Conversely, the motion of the BCE particles is tied to that of the solid bodies, to which they are rigidly attached. Their role is to couple the motion of the SPH particles to the motion of the solid bodies (Hu et al., 2021a).

According to the SPH method, the value of a function $f$ at the position of particle $i$ can be approximated as (Monaghan, 2005):

$$f_i = \sum\nolimits_j f_j W_{ij} \mathcal{V}_j\,, \tag{7}$$

where $W_{ij}$ is a kernel function, and $\mathcal{V}_i$ is the volume of particle $i$, defined as $\mathcal{V}_i = (\sum_j W_{ij})^{-1}$. Thus, the mass associated with particle $i$ can be obtained as $m_i = \rho_i \mathcal{V}_i$. Herein, we use a cubic spline kernel function:

$$W_{ij} = W(\mathbf{r}_{ij}) = \alpha_d \cdot \begin{cases} \frac{2}{3} - R^2 + \frac{1}{2}R^3, & 0 \le R < 1 \\ \frac{1}{6}(2-R)^3, & 1 \le R < 2 \\ 0, & R \ge 2 \end{cases}, \tag{8}$$

for which the relative position between particles $i$ and $j$ is defined as $\mathbf{r}_{ij} = \mathbf{x}_i - \mathbf{x}_j$, with $\mathbf{x}_i$ and $\mathbf{x}_j$ being the positions of particle $i$ and $j$, respectively. For a three-dimensional problem, $\alpha_d = 3/(2\pi h^3)$. The scaled length parameter $R$ is defined as $R = r_{ij}/h$, where $r_{ij}$ is the length of the vector $\mathbf{r}_{ij}$, and $h$ the characteristic smoothing length (one to two times the initial particle spacing $\Delta x$). In the light of Eq. (8), a field variable (e.g., velocity $\mathbf{u}$ or density $\rho$) at the position of particle $i$ receives contributions from the values at all neighbor particles $j$ according to Eq. (7) as long as $j \in \mathcal{N}_{h,i} \equiv \{\mathbf{x}_j : \ r_{ij} < 2h\}$.

For the gradient $\nabla f$ evaluated at the position of SPH particle $i$, both consistent and inconsistent discretizations are available (Fatehi and Manzari, 2011). While computationally slightly more expensive, the consistent SPH discretization

$$\nabla f_i = \sum\nolimits_j (f_j - f_i)\,(\mathbf{G}_i \cdot \nabla_i W_{ij})\,\mathcal{V}_j \ , \tag{9}$$

gives higher accuracy and is used herein. The gradient of the kernel function $W_{ij}$ with respect to the position of particle $i$ is expressed as

$$\nabla_i W_{ij} = \frac{\alpha_d}{h}\frac{\mathbf{r}_{ij}}{r_{ij}} \begin{cases} -2R + \frac{3}{2}R^2, & 0 \le R < 1 \\ -\frac{1}{2}(2-R)^2, & 1 \le R < 2 \\ 0, & R \ge 2 \end{cases}.$$

In Eq. (9), $\mathbf{G}_i \equiv -\left[\sum_j \mathbf{r}_{ij} \otimes \nabla_i W_{ij} \mathcal{V}_j\right]^{-1} \in \mathbb{R}^{3\times 3}$ is a symmetric correction matrix associated with particle $i$. With $\mathbf{G}_i$ being involved in the discretization of the gradient operator, an exact gradient for a linear function $f$ can be guaranteed regardless of the ratio of $h/\Delta x$ (Fatehi and Manzari, 2011), where $\Delta x$ is the initial SPH discretization spacing. This higher accuracy allows one to use a relatively smaller $h$, thus saving computational cost, see, for instance, (Hu et al., 2019).

### 2.3 Overview of the Bayesian inference framework

We express a measured/observed value $y$ as the sum of two components

$$y = \mathcal{G}(\theta) + \varepsilon, \quad \varepsilon \sim N(0, \Gamma) \ , \tag{10}$$

where $\mathcal{G} : \mathcal{X} \mapsto \mathcal{Y}$ denotes a known computer model with unknown parameters $\theta \in \mathcal{X}$; and $\varepsilon$ is assumed to follow a zero-mean normal distribution with a covariance matrix $\Gamma$. Moreover, $\mathcal{X}$ and $\mathcal{Y}$ denote normed vector spaces where $\theta$ and $y$ live in, respectively. The goal is to estimate the posterior distribution $p(\theta|y)$ via Bayesian inference:

$$p(\theta|y) \propto \exp\left(-\frac{1}{2}\|y - \mathcal{G}(\theta)\|_\Gamma^2\right) p(\theta) \ , \tag{11}$$

where $p(\theta)$ is the prior distribution that captures existing knowledge (if any) about the unknown parameters $\theta$. Since a closed form expression for $p(\theta|y)$ is intractable, we fall back on the Metropolis-Hastings algorithm to draw samples from the posterior distribution $p(\theta|y)$.

#### 2.3.1 Metropolis-Hastings

The Metropolis-Hastings (MH) algorithm is a Markov Chain Monte Carlo (MCMC) method for sampling the posterior distribution $p(\theta|y)$ by constructing a Markov chain that is stationary with respect to $p(\theta|y)$. It is

an adaptation of a random-walk with an acceptance/rejection rule to converge to the stationary distribution. The algorithm proceeds by sampling a *proposal* $\theta^*$ from a *proposal distribution*, $J_t(\theta^*, \theta^{t-1})$ at step $t$ (Gelman et al., 1995; Robert, 2015). The proposal is evaluated using the ratio,

$$r = \frac{p(\theta^*|y)/J_t(\theta^*|\theta^{t-1})}{p(\theta^{t-1}|y)/J_t(\theta^{t-1}|\theta^*)} ,$$

and is accepted/rejected using the rule

$$\theta^t = \begin{cases} \theta^*, & \text{with probability } min(r, 1) \\ \theta^{t-1}, & \text{otherwise} \end{cases} .$$

It can be shown that: the Metropolis-Hastings produces a Markov chain with a unique stationary distribution; and this stationary distribution is identical to the target distribution $p(\theta|y)$ (Andrieu et al., 2003).

### 2.3.2 Overview of the software framework for the calibration process

The Bayesian inference process described is well known and relatively straightforward. However, its implementation; i.e., the process of efficiently generating samples out of the posterior distribution, is non-trivial. As such, it is left to third party software, in this case the Python package PyMC (Salvatier et al., 2016).

**Pre-processing:** The higher-fidelity CRM solver in Chrono is used to generate synthetic "experimental" data in order to calibrate the parameters of the lower-fidelity SCM terrain. Details about the data generation process are provided in the following section. The SCM array of unknown parameters is identified as $\theta$. The goal is to identify a choice of low-fidelity model parameters $\theta$ that makes SCM behave similarly to the CRM terrain.

**Sampling:** In this probabilistic programming framework, the low-fidelity SCM model acts as a black-box whose response $\mathcal{G}(\theta)$, shaped by the model parameters calibrated, is made to match as well as possible the synthetic data $y$ generated with CRM. This approach is predicated on the existence of a likelihood function that compares the response of the low-fidelity model with the data in the sampling stage of the Markov Chain. Consistent with the assumption of a Gaussian statistical model (Eq. (10)), we use a Gaussian log likelihood function; i.e., the logarithm of the exponential part in Eq. (11). PyMC offers the flexibility to incorporate this custom log-likelihood function, which in our case takes as input the low-fidelity model response and the "experimental" data. Next, one needs to define prior distributions over the model parameters using standard PyMC functions. In many cases, in the absence of prior knowledge about the distribution of the parameters, one can fall back on uniform distributions. Finally, one has to choose an MC sampler and start running the Markov chain. The sampler then draws the set number of samples based on the defined acceptance probability that is evaluated using the log-likelihood function (Gelman et al., 1995). PyMC eventually returns these samples, along with various sampler stats, as an inference data object that can be used with arviz (Kumar et al., 2019) to do exploratory analysis of the Bayesian model.

# 3 Calibration of the SCM model using a virtual bevameter

While the SPH-backed CRM approach posts RTF values of 30 and above (Hu et al., 2022b), the SCM implementation in Chrono can achieve real-time or close (RTF $\approx 1$). Moreover, the SCM approach in many cases can adequately capture the wheel/implement-soil interaction. However, the parameters tied to the SCM model are usually unknown and need to be first calibrated via a bevameter test (Apfelbeck et al., 2011; Edwards et al., 2017; Mason et al., 2020). The actual bevameter is a self contained unit designed to take in-situ soil strength measurements, usually in conjunction with vehicle mobility modeling and simulation. The bevameter consists of two devices – a plate sinkage device, and an annulus shear device. Since the CRM

parameters are physics based, e.g., Young's modulus, friction angle, we use these parameters to carry out a virtual bevameter test that generates the "experimental" data $y$ in Eq. (10). Using data obtained with the virtual bevameter, we estimated the parameters $\theta$ of the SCM model in a two-step approach. First, data obtained using a virtual bevameter sinkage test is used to calibrate $K_c$, $K_\phi$, and $n$ in Eq. (1); these parameters affect the wheel-soil normal contact force. Subsequently, we calibrate the other three parameters ($c$, $\varphi$, and $K_s$ in Eqs. (2) and (3)) for the tangential force evaluation using data obtained from the annulus shear test.

### 3.1 Plate sinkage test

In this test, the plate was pressed down into the soil with a constant vertical velocity, see snapshot shown in Fig. 1. The plate and connecting bar were modeled as a rigid multibody system which interacted with the CRM soil. The density and frictional coefficient of the deformable soil were 1700 kg/m$^3$ and 0.7, respectively. The cohesion coefficient of the soil was set as 1000 Pa. There were two different rigid plates used in this test, of radii 20 cm and 30 cm. For the smaller plate, the size of the soil bin was 1.0 m × 1.0 m × 0.6 m; for the larger plate, the soil bin's size was increased to 1.2 m × 1.2 m × 0.6 m to avoid wall boundary effects. Each plate was pressed down with three constant velocities: 0.5 cm/s, 1.0 cm/s, and 2.0 cm/s, in three separate simulations.

Figures 2 (a) and (b) report pressing force versus sinkage curves for three plate vertical velocities. It is noted that the three curves are almost identical regardless of the plate enforced speed. To obtain the calibration data from these experiments, we selected eight points corresponding to different plate sinkages, see red squares in Fig. 2 and results in Table 1. The data in Table 1 was treated as "experimental" data in the subsequent calibration of $K_c$, $K_\phi$, and $n$.

Table 1: Pressing force vs. sinkage data collected from the high-fidelity CRM simulations.

| Sinkage (m) | 0.025 | 0.05 | 0.075 | 0.1 | 0.125 | 0.15 | 0.175 | 0.2 |
|---|---|---|---|---|---|---|---|---|
| Force (N) - Small plate | 3799 | 7071 | 10279 | 13684 | 17196 | 21147 | 25217 | 30017 |
| Force (N) - Large plate | 7699 | 15174 | 23344 | 31774 | 41468 | 52260 | 63791 | 77502 |

The likelihood function of the Markov chain process was evaluated as follows: given a set of $K_c$, $K_\phi$, and $n$, an SCM simulation was run and the force-vs-sinkage values were recorded at the eight chosen sinkages. These force values were compared against the CRM values associated with the eight sinkages. Specifically, the likelihood function was defined as

$$\mathbb{L} = -\frac{1}{2\sigma^2}\sum_{k=1}^{N}\frac{\left[F^{obs}(k) - F(k)\right]^2}{N}\,, \tag{12}$$

where $N$ is the total number of observed data for each plate, which is 16 here – eight for each plate; $F^{obs}(k)$ is the observed force at each sinkage shown in Table 1; $F(k)$ is the evaluated force using the sampled $K_c$, $K_\phi$, and $n$ parameters at sinkage $k$; and $\sigma^2$ is the variance we would like to see between data and our model output (herein set to 0.01). To obtain a converged distribution of $K_c$, $K_\phi$, and $n$, the total number of samples varied from 10 000 to 500 000 in four separate cases. In each of the four cases, we also run four Metropolis-Hastings chains in parallel. It must also be noted that we sample more than the stated number of samples and discard $\frac{n_{steps}}{n_{chains}+1}$ samples where $n_{steps}$ is the number of samples required, and $n_{chains}$ is the number of chains run in parallel. This is a standard approach used to reduce the influence of our starting points in prior space and is called *warm-up* (Gelman et al., 1995). We assess the convergence of the posterior distributions by visual inspection of the trace of the four chains combined with a reading of the split-$\hat{R}$ metric, which is a commonly used convergence diagnostic procedure (Vehtari et al., 2021). Figures 3, 5, 7 show the posterior distributions of $K_c$, $K_\phi$, and $n$ after different numbers of samples. The more points sampled, the smoother

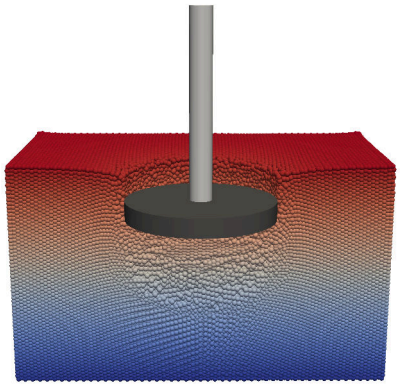

(a) 20 cm plate with plate on

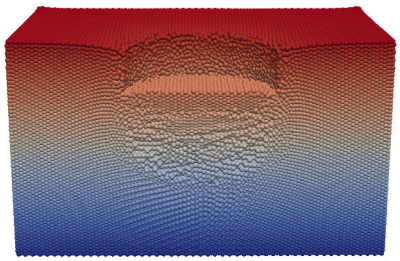

(b) 20 cm plate with plate off

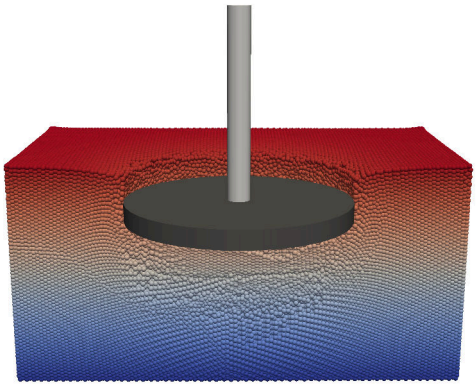

(c) 30 cm plate with plate on

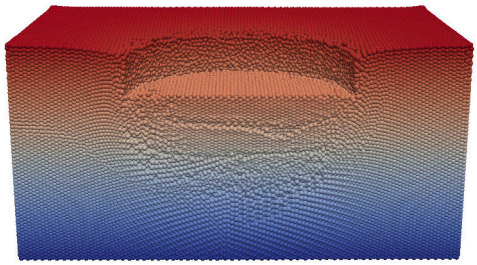

(d) 30 cm plate with plate off

Figure 1: Plate sinkage tests using the virtual bevameter with different plate sizes; the vertical speed was constant during each test.

the posterior. In the 500 000 samples case, i.e. Figs. 3, 5, 7 (d), the mean values of $K_c$, $K_\phi$, and $n$ exponent are -1.1e5, 2.2e6, and 1.2, respectively. Figures 4, 6, 8 show the posterior distribution and trace plot in four different Metropolis-Hastings chains. It can be seen that the four chains that start from random points in the prior parameter space all converge to a similar posterior. Table 2 provides the split-$\hat{R}$ for $K_c$, $K_\phi$, and $n$. Given that all three values are less than 1.01, the calibration process is deemed as converged (Vehtari et al., 2021). Note that the Monte Carlo Standard Error (normalized with the posterior mean), which helps one quantify the sampler error (Flegal et al., 2008; Vehtari et al., 2021), is sufficiently small.

To test the goodness of the parameters obtained, we ran a pressing force experiment again using the mean values of the three parameters and Eq. (1) for the two plates at each sinkage. The results were compared against the original observed data obtained from the simulations using the CRM method. Figures 9 (a) and (b) show the comparison for the plates with different size. The results evaluated using the SCM model and the calibrated parameters match well with the original high-fidelity simulation results.

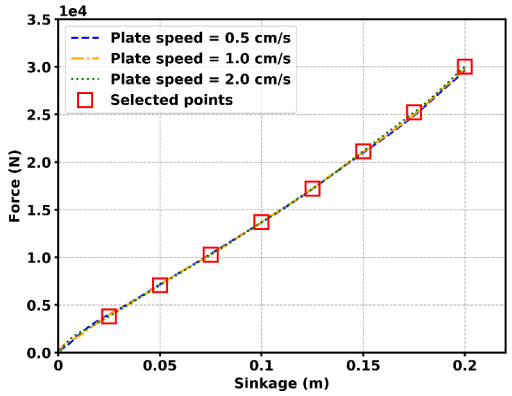


(a) Small plate ($r = 20$ cm)

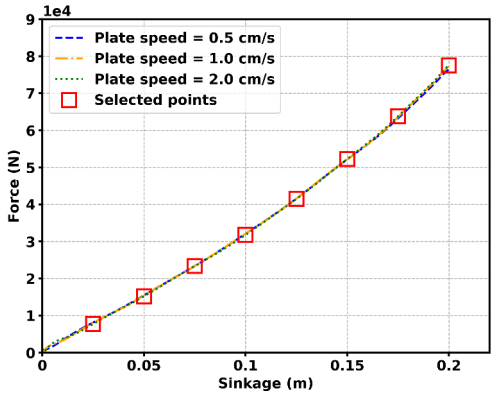


(b) Large plate ($r = 30$ cm)

Figure 2: Pressing force vs. plate sinkage curves with different plate vertical velocity. The selected values (in red boxes) provide average data used in calibration.

Table 2: Normalized error and convergence metrics for calibration of $K_c$, $K_\phi$, and $n$ – 500 000 samples.

| Parameters | $\mu_{MCSE}$ | $\sigma_{MCSE}$ | $\hat{R}$ |
|---|---|---|---|
| $K_c$ | 1.31e-3 | 8.33e-4 | 1.00039 |
| $K_\phi$ | 4.8e-4 | 3.4e-4 | 1.00072 |
| $n$ | 1.49e-4 | 1.08e-4 | 1.00076 |

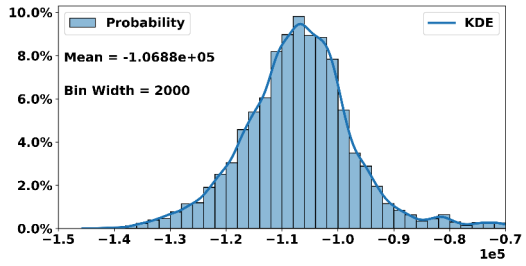


(a) 10 000 samples

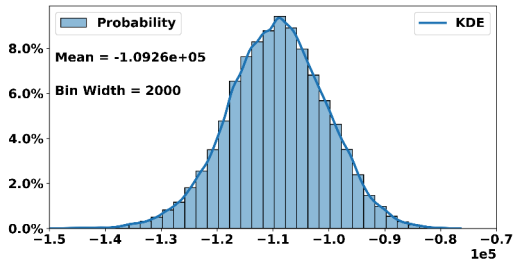


(b) 50 000 samples

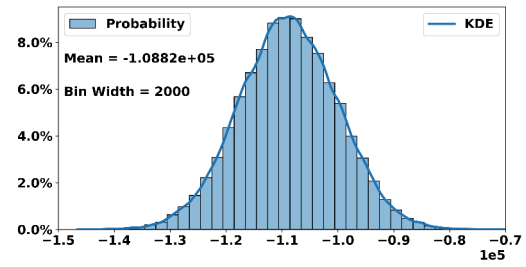


(c) 100 000 samples

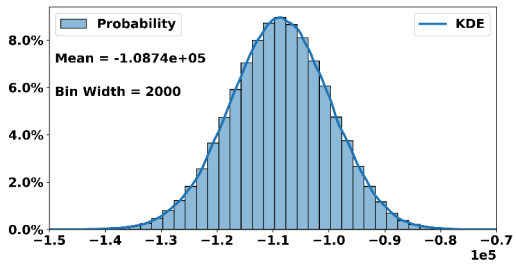


(d) 500 000 samples

Figure 3: Averaged posterior probability distribution and its kernel density estimation (KDE) of four chains for the parameter $K_c$ with different number of samples.

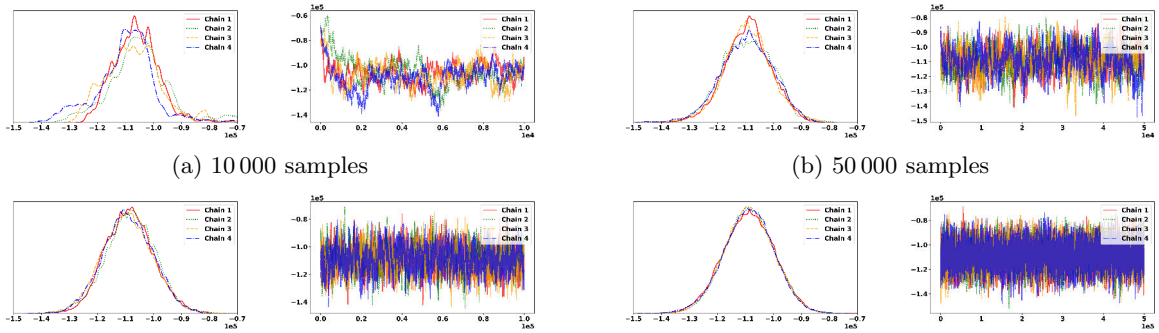


(a) 10 000 samples (b) 50 000 samples

(c) 100 000 samples (d) 500 000 samples

Figure 4: Posterior probability distribution and trace plot of parameter $K_c$ in four different Metropolis-Hastings chains.

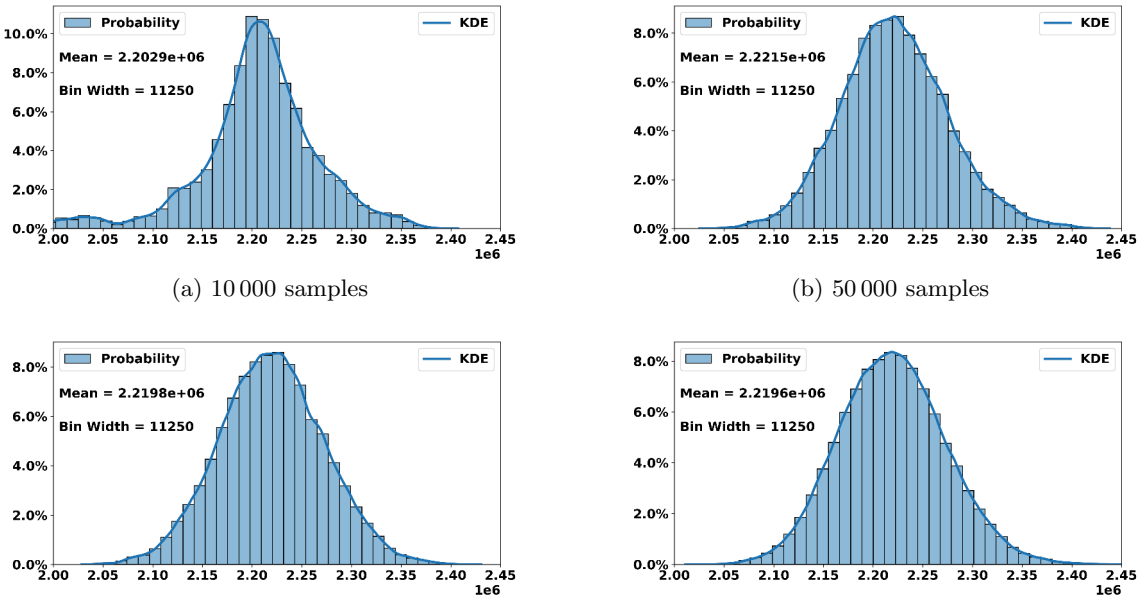


(a) 10 000 samples (b) 50 000 samples

(c) 100 000 samples (d) 500 000 samples

Figure 5: Averaged posterior probability distribution and its kernel density estimation (KDE) of four chains for the parameter $K_\phi$ with different number of samples.

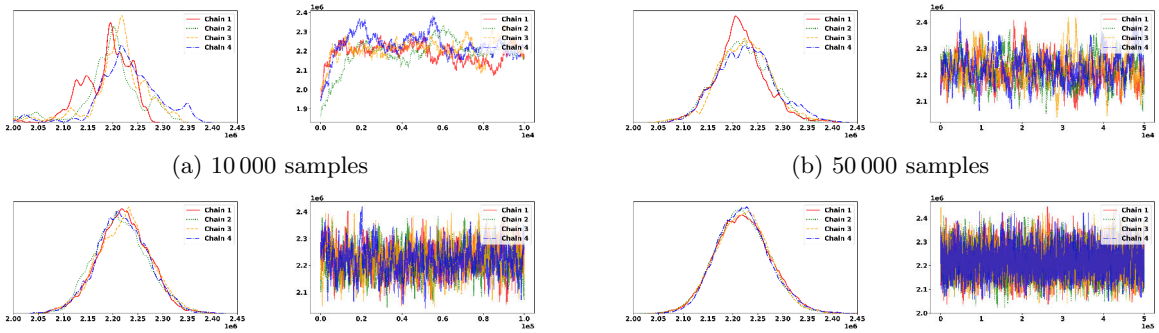


(a) 10 000 samples (b) 50 000 samples

(c) 100 000 samples (d) 500 000 samples

Figure 6: Posterior probability distribution and trace plot of parameter $K_\phi$ in four different Metropolis-Hastings chains.

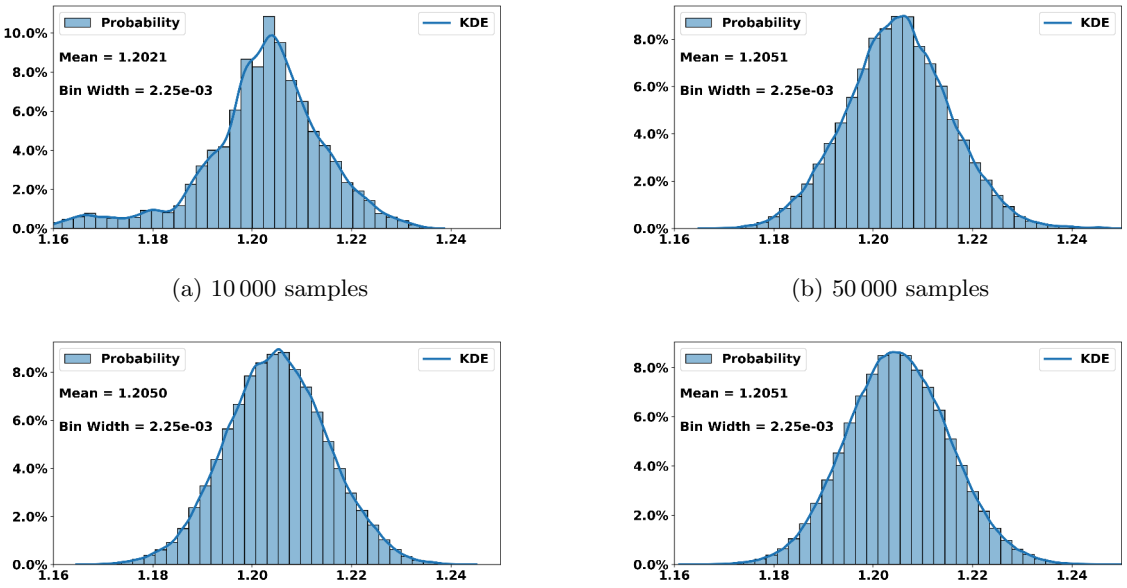


(a) 10 000 samples (b) 50 000 samples

(c) 100 000 samples (d) 500 000 samples

Figure 7: Averaged posterior probability distribution and its kernel density estimation (KDE) of four chains for the parameter $n$ with different number of samples.

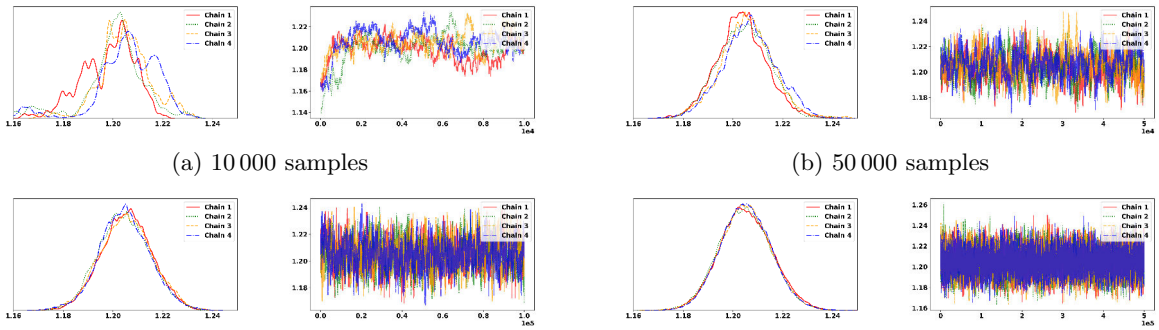


(a) 10 000 samples (b) 50 000 samples

(c) 100 000 samples (d) 500 000 samples

Figure 8: Posterior probability distribution and trace plot of parameter $n$ in four different Metropolis-Hastings chains.

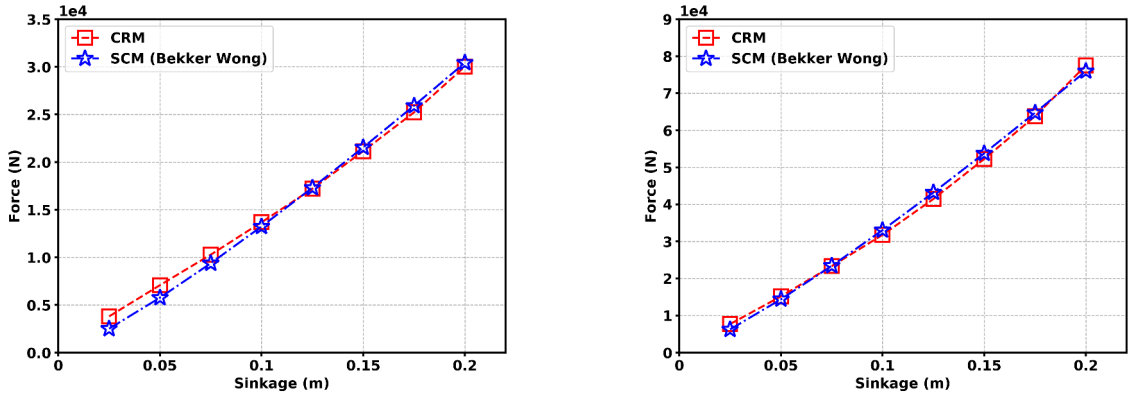


(a) Small plate ($r = 20$ cm) (b) Large plate ($r = 30$ cm)

Figure 9: A comparison between selected points using CRM model and SCM model. The SCM results are calculated using calibrated values of $K_c$, $K_\phi$, and $n$ and the Bekker-Wong formulation in Eq. (1).

### 3.2 Annulus shear test

The annulus shear test is performed to calibrate the cohesion coefficient $c$, frictional coefficient $\varphi$, and the Janosi coefficient $K_s$, see Eqs. (2) and (3). To that end, the annulus was first pressed down into the CRM soil with a constant load in the vertical direction, and then rotated with a constant angular velocity (1 deg/s), see snapshot in Fig. 10. The inner and outer radii of the annulus were 15 cm and 20 cm. The density and frictional coefficient of the soil were those from the plate sinkage tests, i.e., 1700 kg/m$^3$ and 0.7, respectively. The size of the soil bin was 1.0 m $\times$ 1.0 m $\times$ 0.2 m. To generate sufficient "experimental" data from the simulations, the annulus was rotated under different loads (varied from 25 kg to 200 kg with Earth gravity) in eight separate tests.

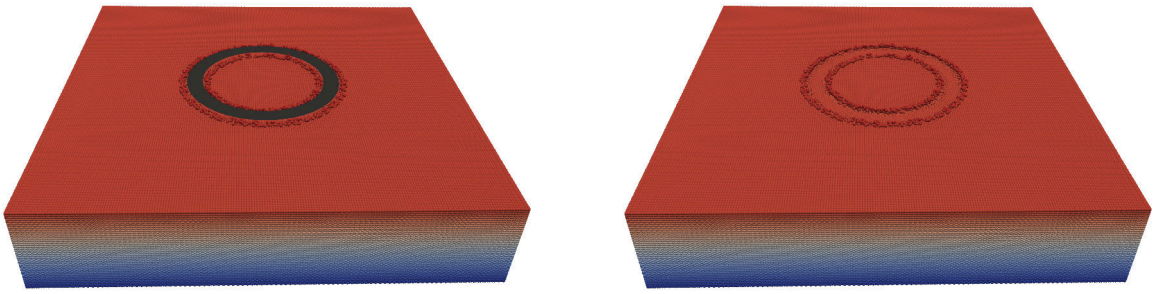

(a) 20 cm annulus with annulus on

(b) 20 cm annulus with annulus off

Figure 10: Annulus shear test using virtual bevameter. Rotation speed was fixed at 1 deg/s; normal load varied from 25 kg to 200 kg.

Figure 11 reports the amount of torque that needed to be applied over time to maintain, under different loads, an annulus angular velocity of 1 deg/s. All simulations were 12 s long to ensure that a steady state was reached. The results indicate that the higher the load, the larger the torque needed to rotate the annulus with a fixed angular velocity. The "experimental" data was collected for different loads at several time instances. First, we measured the torque when the steady states were reached, see Table 3. This data was used to calibrate the parameters $c$ and $\varphi$ of Eq. (3). Then, we measured the torque before the steady state and used them to calibrate the Janosi coefficient $K_s$. Using Fig. 11 for reference, the data was collected at $t =$ 1s, 2s, and 3s, and reported in Table 4.

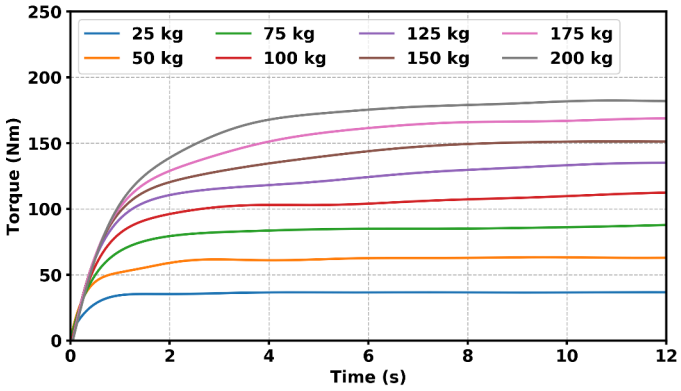


Figure 11: Time histories of the total torque applied on the annulus under different loads.

The SCM parameters $c$, $\varphi$, and $K_s$ were sampled using the approach described in Sections 2.3.1 and 2.3.2. However, unlike in the previous section, the three parameters were calibrated in two steps. First, $c$ and $\varphi$

Table 3: Vertical load vs. rotation torque data collected from the CRM simulations.

| Load (kg) | 25 | 50 | 75 | 100 | 125 | 150 | 175 | 200 |
|---|---|---|---|---|---|---|---|---|
| Torque (N·m) | 36 | 62 | 84 | 105 | 124 | 141 | 157 | 170 |

Table 4: Vertical load vs. rotation torque data collected from the CRM simulations.

| Load (kg) | 25 | 50 | 75 | 100 | 125 | 150 | 175 | 200 |
|---|---|---|---|---|---|---|---|---|
| Torque at 1 s (N·m) | 34 | 52 | 68 | 82 | 92 | 98 | 101 | 104 |
| Torque at 2 s (N·m) | 35 | 59 | 79 | 96 | 111 | 120 | 129 | 139 |
| Torque at 3 s (N·m) | 36 | 62 | 82 | 102 | 116 | 129 | 142 | 157 |

were calibrated using the data in Table 3. Subsequently, $K_s$ was calibrated using the data in Table 4. During the calibration process, for each parameter sample, the torque was evaluated using Eqs. (2) and (3). The likelihood function was defined as

$$\mathbb{L} = -\frac{1}{2\sigma^2} \sum_{k=1}^{N} \frac{\left[T^{obs}(k) - T(k)\right]^2}{N} , \tag{13}$$

where $N$ is the number of data points; $T^{obs}(k)$ is the observed torque under each load shown in Tables 3 and 4; $T(k)$ is the evaluated torque using the sampled parameters; and $\sigma^2$ was set to 0.01. The total number of iterations varied from 10 000 to 500 000 in four separate cases, with each case using four different Metropolis-Hastings chains running in parallel. Figures 12, 14, and 16 show the posterior distribution of $c$, $\varphi$, and $K_s$ after different number of iterations. As expected, the more points sampled, the smoother the curves. In the case with 500 000 samples, i.e. Figs. 12, 14, and 16 (d), the mean values of $c$, $\varphi$, and $K_s$ were 2495, 24, and 2.95e-3, respectively. Figures 13, 15, and 17 show the posterior distribution and trace plot of four different Metropolis-Hastings chains. Table 5 shows the split-$\hat{R}$ for $c$ and $\varphi$; Table 6 does the same for $K_s$. In both cases, the calibration processes are deemed as converged.

Table 5: Normalized error and convergence metrics for $c$ and $\varphi$ calibration – 500 000 samples

| Parameters | $\mu_{MCSE}$ | $\sigma_{MCSE}$ | $\hat{R}$ |
|---|---|---|---|
| $c$ | 4.14e-4 | 2.93e-4 | 1.0001 |
| $\varphi$ | 9.1e-5 | 6.5e-5 | 1.0001 |

To test the goodness the calibrated parameters, we evaluated the torque again using the mean values of the three parameters and Eq. (3) for the annulus under different loads. The results were compared against the original observed data obtained from the simulations using the CRM method. Figure 18 shows the comparison between the CRM simulations and the SCM model with calibrated parameters.

Table 7 reports values for all six SCM parameters calibrated via Bayesian inference using data generated by a virtual bevameter test with CRM terrain. The approach used is summarized in Fig. 19. From a high vantage point, the methodology has three steps: (*i*) generate "experimental" data through simulation using a virtual bevameter in conjunction with CRM terrain; (*ii*) calibrate the SCM parameters using Bayesian inference; (*iii*) validate the calibrated parameters using simulations of single wheel and full VIPER rover using both SCM and CRM terrains. The latter point is discussed in the next section.

Table 6: Normalized error and convergence metrics for $K_s$ calibration – 500 000 samples.

| Parameters | $\mu_{MCSE}$ | $\sigma_{MCSE}$ | $\hat{R}$ |
|---|---|---|---|
| $K_s$ | 1e-6 | 5e-7 | 1.00001 |

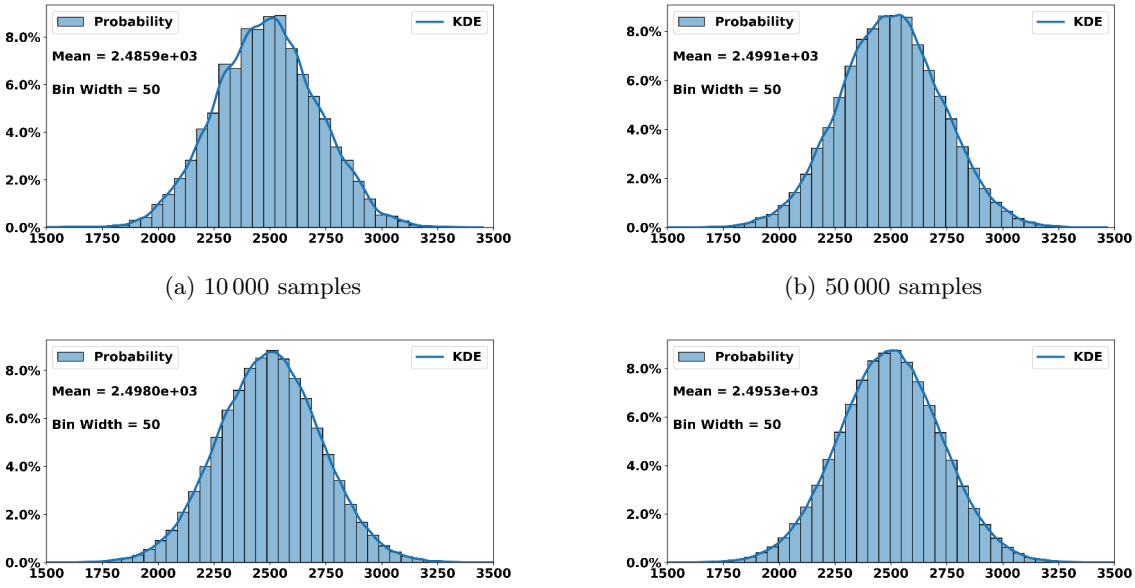


(a) 10 000 samples

(b) 50 000 samples

(c) 100 000 samples

(d) 500 000 samples

Figure 12: Averaged posterior probability distribution and its kernel density estimation (KDE) of four chains for the parameter $c$ with different number of samples.

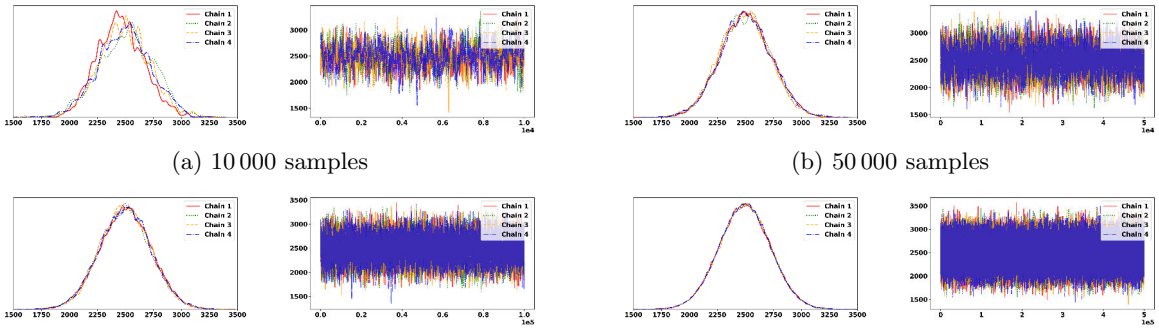


(a) 10 000 samples

(b) 50 000 samples

(c) 100 000 samples

(d) 500 000 samples

Figure 13: Posterior probability distribution and trace plot of parameter $c$ in four different Metropolis-Hastings chains.

Table 7: Calibrated values of the SCM parameters using data generated from CRM simulations.

| SCM parameter | $K_c$ (N/m$^{n+1}$) | $K_\phi$ (N/m$^{n+2}$) | $n$ | $c$ (Pa) | $\varphi$ (deg) | $K_s$ (m) |
|---|---|---|---|---|---|---|
| Calibrated value | -1.1e5 | 2.2e6 | 1.2 | 2495 | 24 | 2.95e-3 |

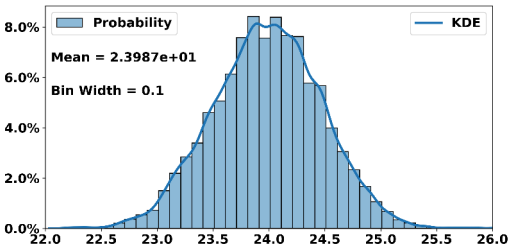


(a) 10 000 samples

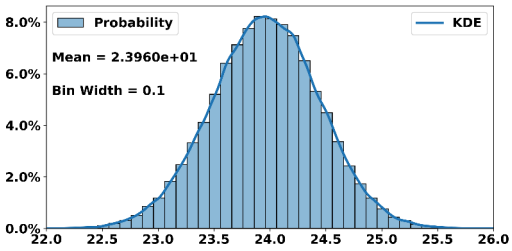


(b) 50 000 samples

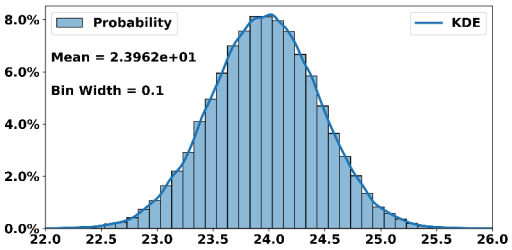


(c) 100 000 samples

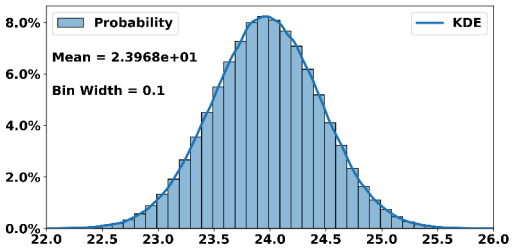


(d) 500 000 samples

Figure 14: Averaged posterior probability distribution and its kernel density estimation (KDE) of four chains for the parameter $\varphi$ with different number of samples.

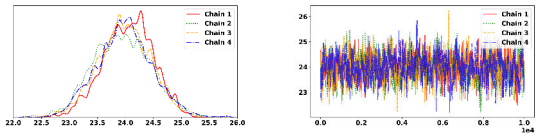

(a) 10 000 samples

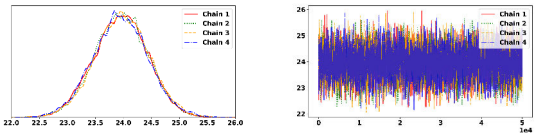

(b) 50 000 samples

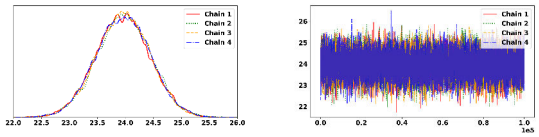

(c) 100 000 samples

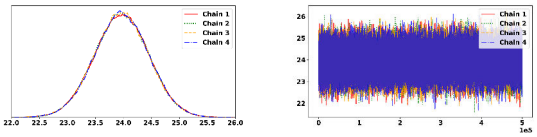

(d) 500 000 samples

Figure 15: Posterior probability distribution and trace plot of parameter $\varphi$ in four different Metropolis-Hastings chains.

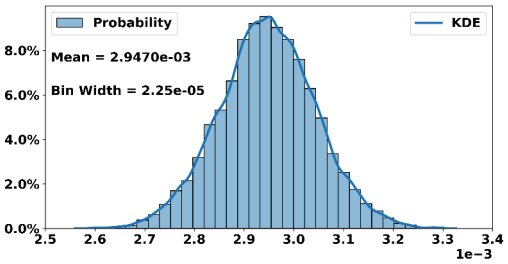


(a) 10 000 samples

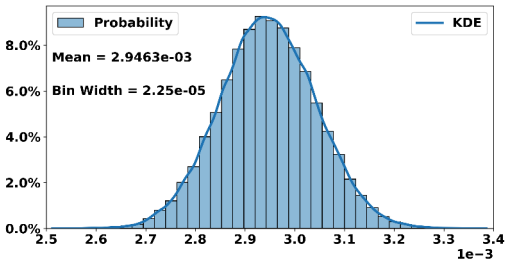


(b) 50 000 samples

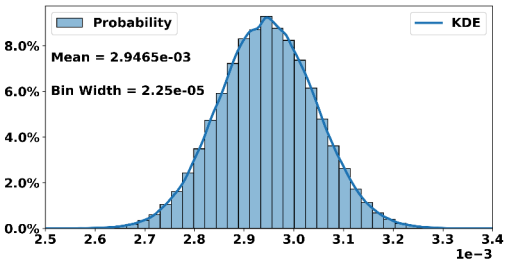


(c) 100 000 samples

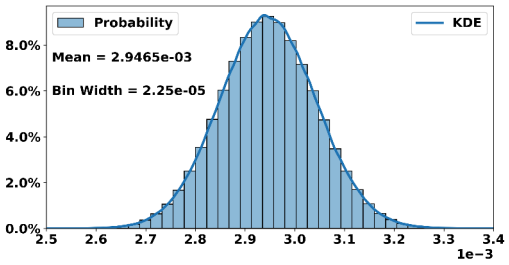


(d) 500 000 samples

Figure 16: Averaged posterior probability distribution and its kernel density estimation (KDE) of four chains for the parameter $K_s$ with different number of samples.

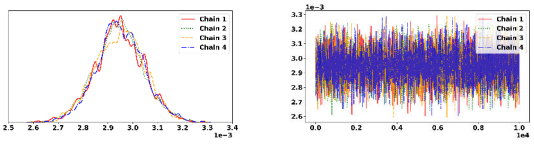


(a) 10 000 samples

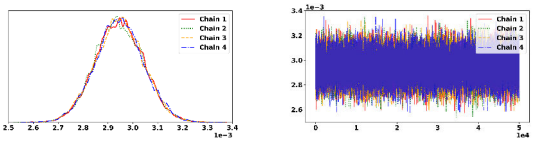


(b) 50 000 samples

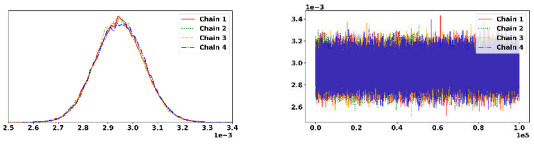


(c) 100 000 samples

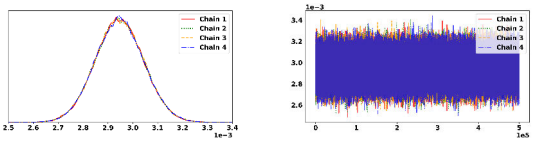


(d) 500 000 samples

Figure 17: Posterior probability distribution and trace plot of parameter $K_s$ in four different Metropolis-Hastings chains.

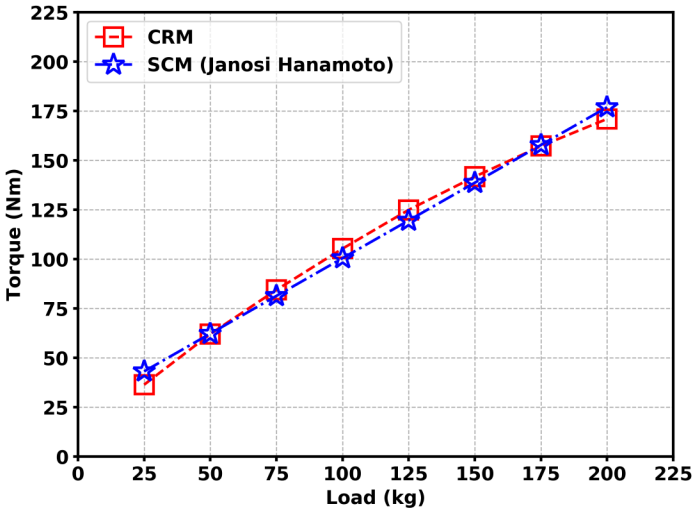


Figure 18: A comparison between selected points using CRM model and SCM model. The SCM results are calculated using calibrated values of $c$, $\varphi$, and $K_s$ and the Janosi formulation in Eq. (3).

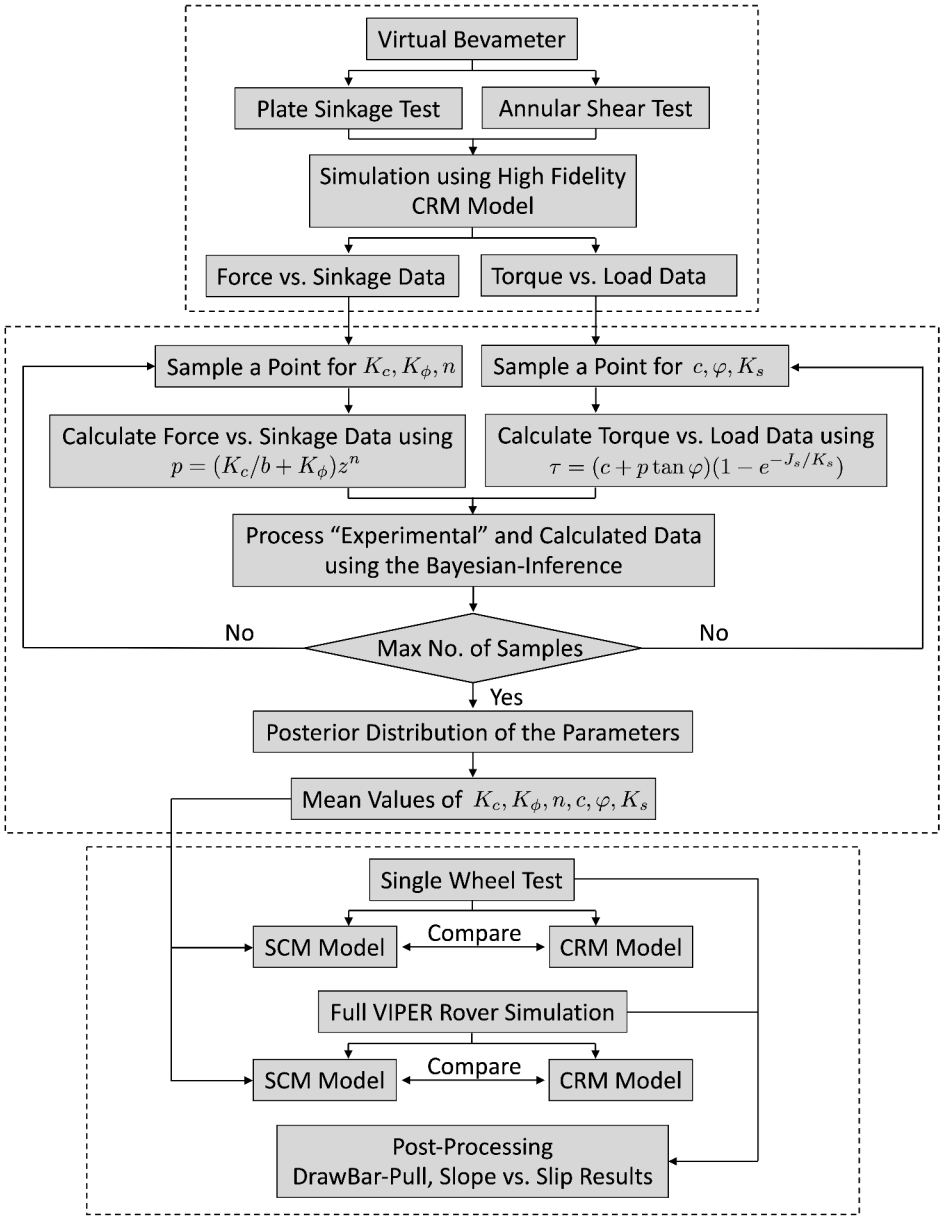


Figure 19: Flowchart of the approach proposed that draws on three stages: (*i*) data generation using a virtual bevameter; (*ii*) parameter calibration using Bayesian inference; (*iii*) validation using single wheel and full rover simulations.

# 4 Validation of the calibrated SCM model

The SCM parameters obtained using the virtual bevameter test are used in this section to conduct single wheel and full VIPER rover simulations. The SCM and CRM simulation results compared are the DrawBar-Pull force and terrain slope that the wheel/rover is able to negotiate.

## 4.1 Single wheel validation

The single wheel was moved under a controlled slip and normal loading conditions within a confined soil bin, see Fig. 20. The wheel, which has no grousers or other features, moved with a constant velocity $v = 0.25$ m/s. Given a slip ratio $s$, the wheel angular velocity is obtained as $\omega = \frac{v}{r(1-s)}$, where $r$ is the radius of the wheel. In the first test, a rigid HMMWV wheel was used with a width of $w = 0.25$ m and a radius of $r = 0.47$ m. The SCM parameters are as in Table 7. The single wheel test was run with slip ratios from 0 to 0.8. The simulations were long enough to reach steady state. The SCM DrawBar-Pull force and the equivalent terrain slope that the wheel can climb were measured and compared with the high-fidelity CRM simulations, see Fig. 21. It is noted that all simulation were performed on a flat terrain although a slope is reported. The equivalent terrain slope was calculated as $slope = \arctan(dbp/load)$, where $dbp$ is the DrawBar-Pull force at a given slip ratio, and $load$ is 108 kg; the experiment was conducted under Earth gravity. Figure 22 shows the time histories of the DrawBar-Pull force with different slip ratios. Both SCM and CRM simulations reached a steady state; the SCM results were noted as more noisy. Figure 23 shows the simulation results obtained using the CRM approach with wheel position and the particle distributions of the terrain. It is noted that the higher the slip ratio, the more wheel sinkage is observed. A higher slip ratio also led to more soil stick to the wheel surface due to cohesion.

The same test on the same terrain was run with a rover wheel with geometry similar but not identical to that of VIPER's (grouser size of 7 mm). The width of the wheel was $w = 0.29$ m and the radius was $r = 0.25$ m. The SCM and CRM DrawBar-Pull force and equivalent terrain slope are shown in Fig. 24. The results indicate good agreement despite the presence of the shallow grousers. The time histories of the DrawBar-Pull force obtained from SCM are more noisy than those previously obtained for the rigid HMMWV wheel, see Fig. 25. Finally, Fig. 26 shows snapshots of the CRM simulation.

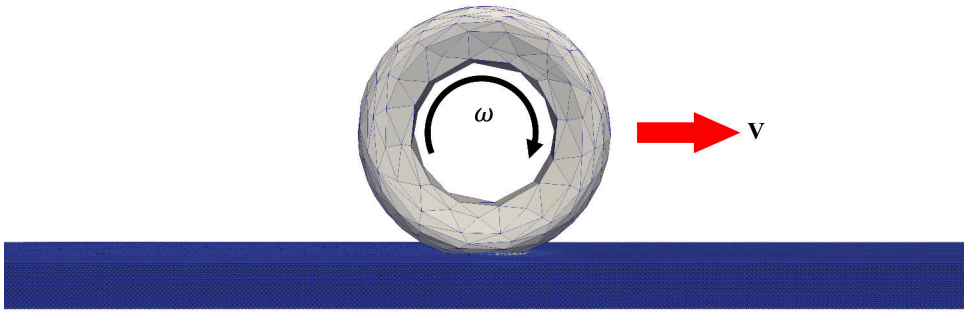


Figure 20: Single rigid wheel test setup.

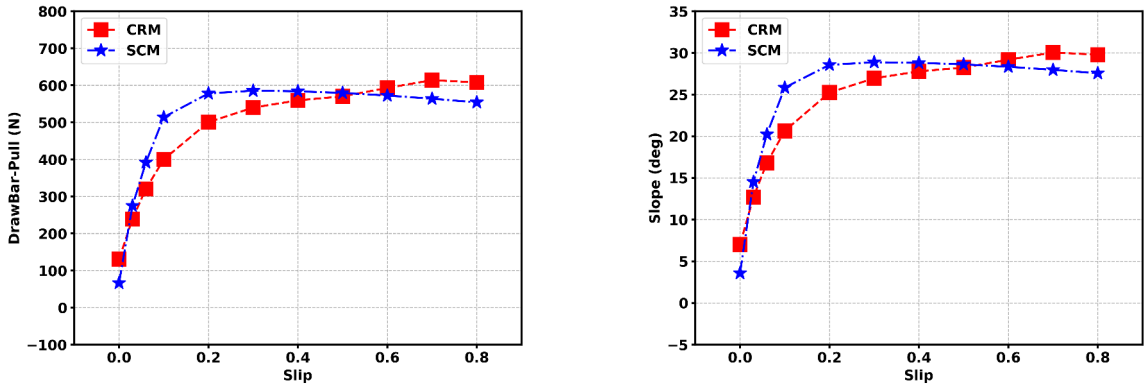


(a) DrawBar-Pull force

(b) Terrain slope

Figure 21: Single wheel test (rigid HMMWV wheel): DrawBar-Pull force and terrain slope vs. slip ratio curves for a normal load associated with 108 kg under Earth gravitational pull. The SCM simulation was run with parameters from Table 7.

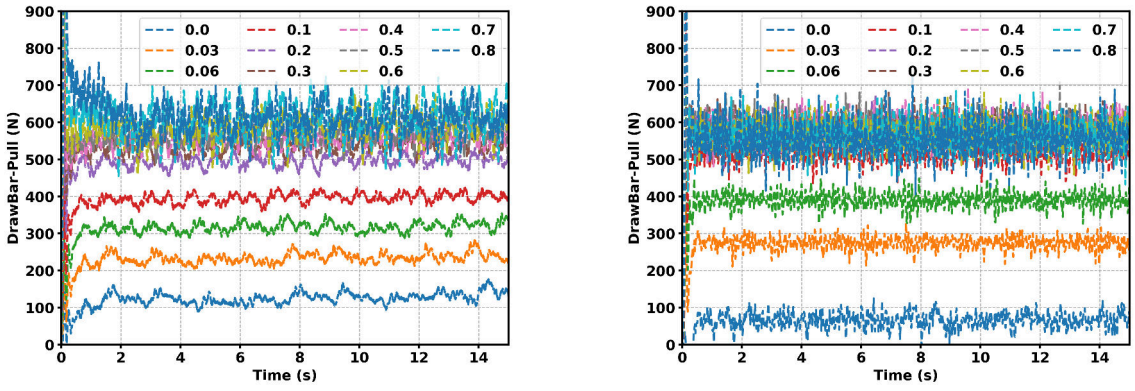


(a) CRM

(b) SCM

Figure 22: Single wheel test (rigid HMMWV wheel): Time histories of DrawBar-Pull force with different wheel slip ratio.

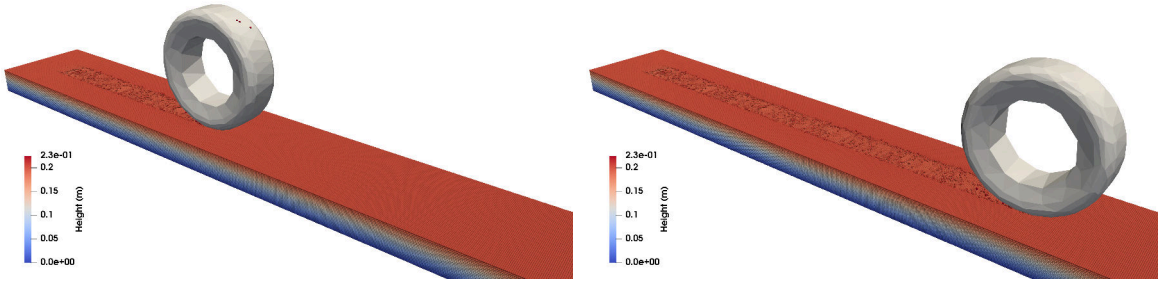


(a) slip = 0

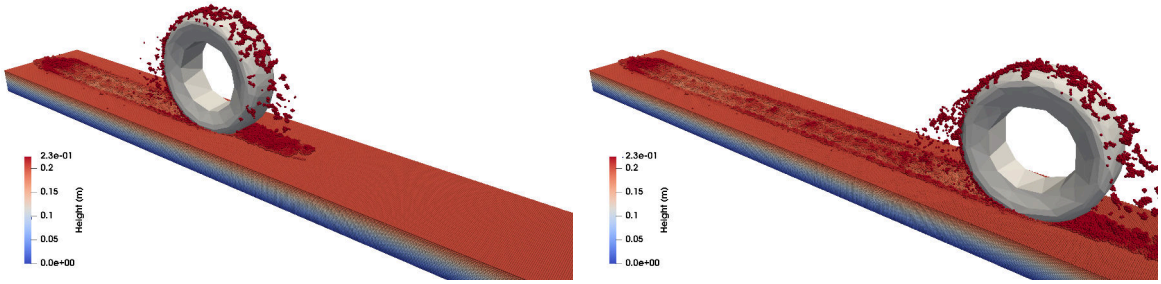


(b) slip = 0.8

Figure 23: Wheel (rigid HMMWV wheel) positions and SPH particle distributions of the CRM terrain with different wheel slips.

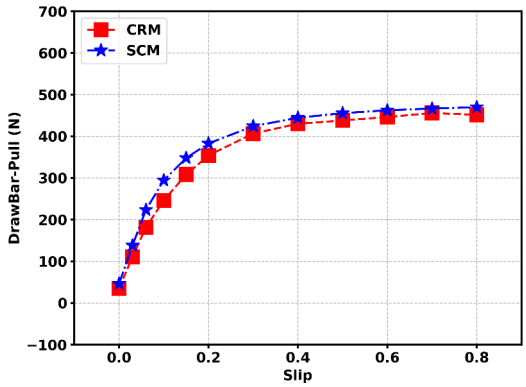


(a) DrawBar-Pull force

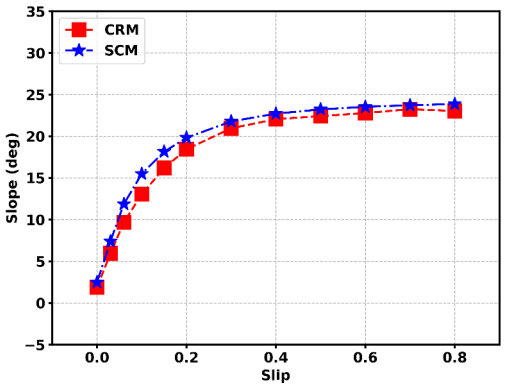


(b) Terrain slope

Figure 24: Single wheel test (VIPER wheel): DrawBar-Pull force, terrain slope vs. slip ratio curves for a normal load of 108 kg under Earth gravitational pull. The SCM simulation was run with mean value of the parameters from the posterior distribution.

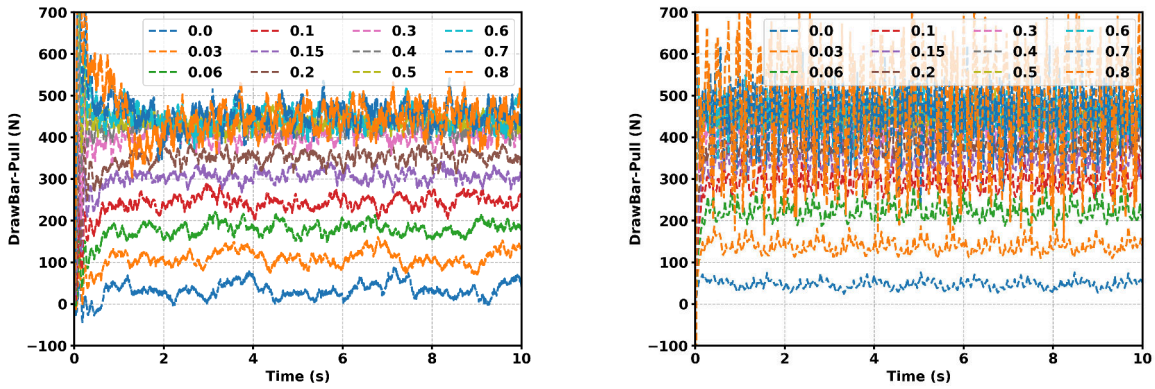


(a) CRM (b) SCM

Figure 25: Single wheel test (VIPER wheel): Time histories of DrawBar-Pull force with different wheel slip ratio.

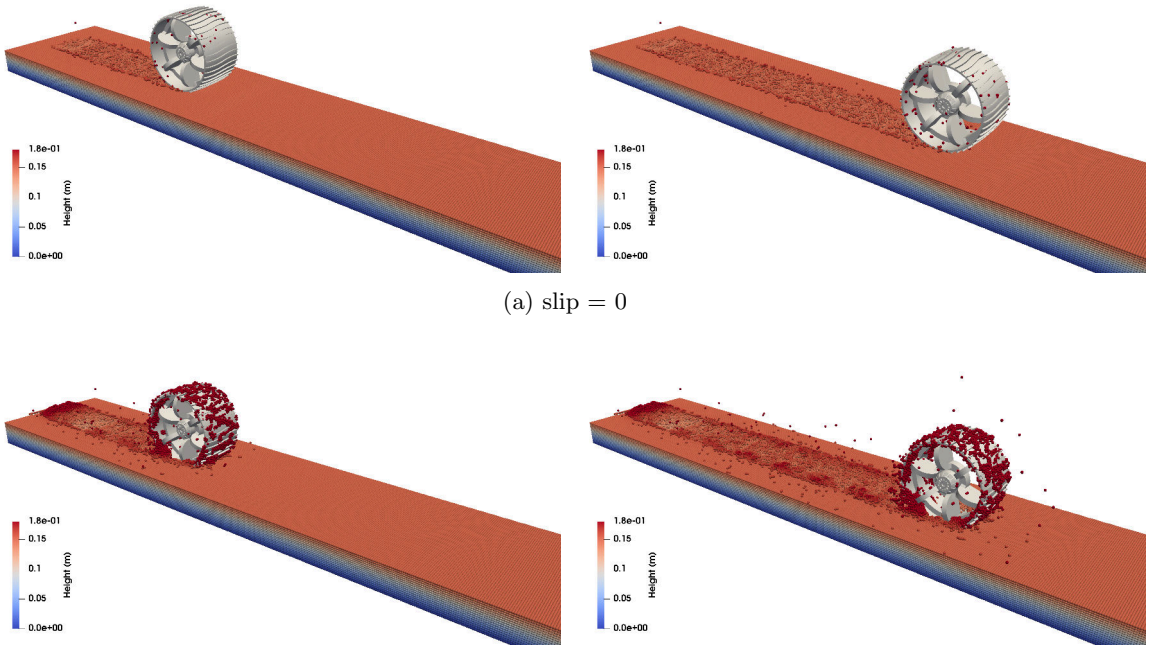


(a) slip = 0

(b) slip = 0.8

Figure 26: VIPER wheel: SPH particle distributions of the CRM terrain for different wheel slips.

### 4.2 Full vehicle validation

In this last test, the calibrated SCM terrain was used for a full rover simulation and the results were compared against the ones obtained with a CRM terrain. There are two reasons why this experiment was run: (*i*) the mechanical system was more complicated; (*ii*) the front wheels moved on undisturbed terrain, while the rear ones experienced terrain that was disturbed by the front wheels. The vehicle used was a replica of the Moon VIPER rover with the wheel tested above. The total mass of the rover was 430 kg, which was roughly four times the load of the single wheel in the previous section. We used the mean values of the six parameters (shown in Table 7) obtained using the virtual bevameter-based calibration.

The vehicle was initially placed on the flat deformable terrain with a carriage connected to the chassis of the rover. The carriage can move in the horizontal direction with constant velocity $v = 0.25$ m/s. The four wheels were also driven with a constant angular velocity. By adjusting the angular velocity $\omega$, the slip ratio of the wheel can be controlled from 0 to 0.8. We measured the DrawBar-Pull force and the equivalent terrain slope that the rover can climb under a given wheel slip (see Fig. 27 (a) and (b)). The low-fidelity SCM results match well the higher-fidelity CRM ones. Figure 28 gives the time histories of the DrawBar-Pull force that are applied on the full rover; the results are noisy, as observed in the single wheel test. Comparing the results in Figs. 24 and 27, we conclude that the DrawBar-Pull force in the full rover simulation is roughly four times that in the single wheel test. Figure 29 shows several snapshots of the rover position and the corresponding particle distributions for the CRM terrain.

The terrain in the CRM simulations was made up of 3 million SPH particles. To simulate one second of the motion of the rover, CRM required 90 s of compute time; the SCM took about 4 s. In other words, the RTF gap between SCM and CRM is approximately 20, although the results for this simple test are comparable. In other words, when SCM represents a viable terramechanics alternative; i.e., for simple wheel geometry, low to moderate shear, and low sinkage, it runs one order of magnitude faster than CRM.

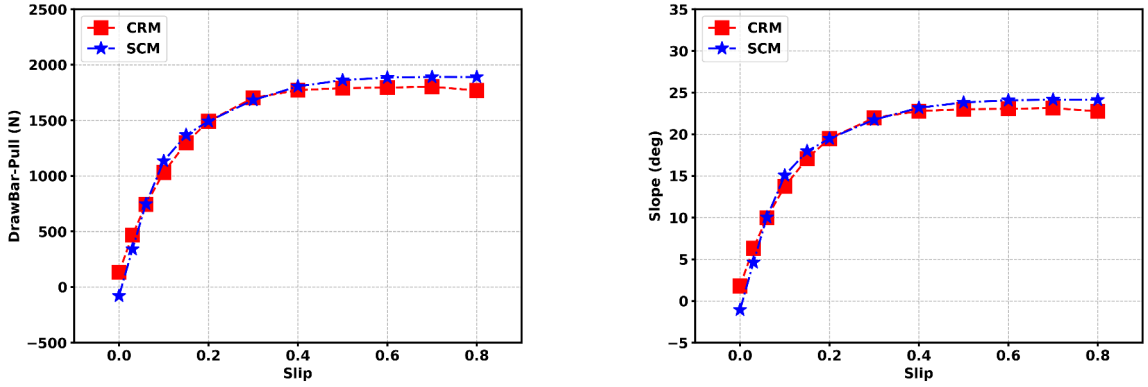


(a) DrawBar-Pull force

(b) Terrain slope

Figure 27: Full vehicle simulation: DrawBar-Pull force, terrain slope vs. slip ratio curves. The SCM simulation was running with mean value of the parameters from the posterior distribution.

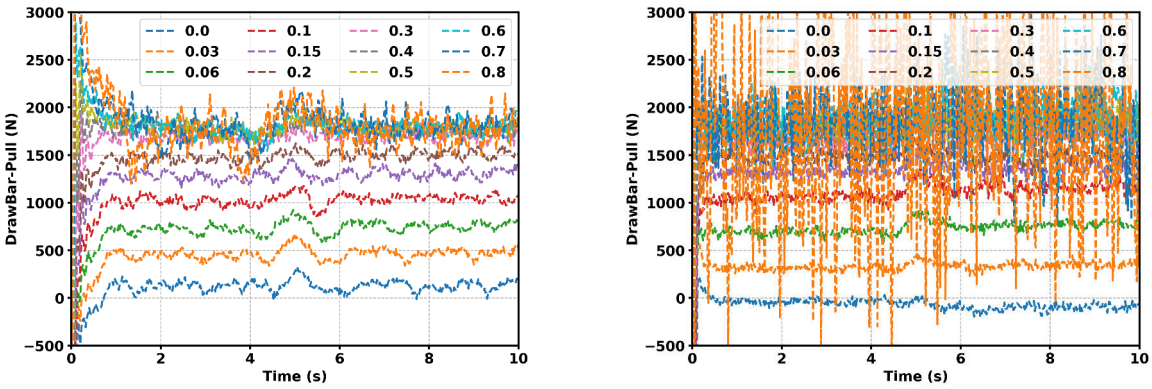


(a) CRM (b) SCM

Figure 28: Full VIPER rover simulation: Time histories of DrawBar-Pull force with different wheel slip ratio.

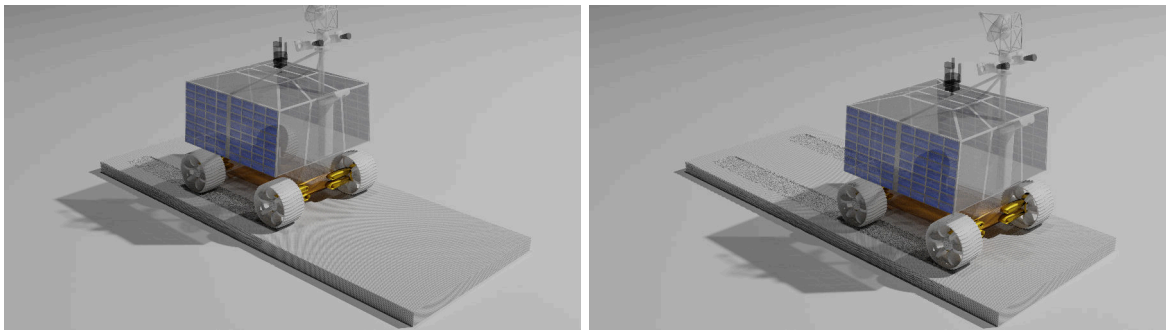

(a) slip = 0

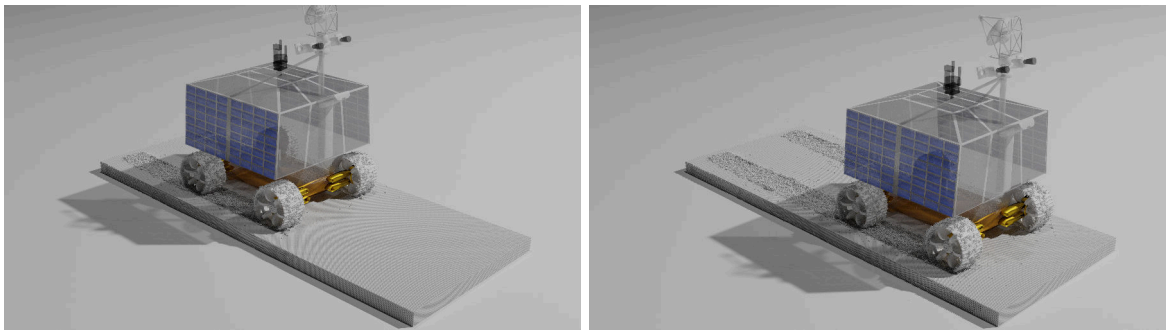

(b) slip = 0.8

Figure 29: Rover positions and SPH particle distributions of the terrain with different wheel slips modeled using CRM approach.

# 5 Conclusion

This contribution promotes the idea of using terramechanics virtual tests to calibrate lower fidelity terrain models that can be subsequently used for mobility analysis purposes. In this context, we outline a Bayesian calibration approach that produces the model parameters associated with a deformable SCM terrain. The highlight of the proposed methodology is tied to the observation that since a bevameter test necessary for SCM calibration is not straightforward to carry out, we employ a high-fidelity deformable terrain model to carry out the bevameter test in simulation. To that end, a CRM terrain is used to produce calibration "experimental data". Upon model calibration, the SCM terrain yields results similar to the ones obtained with a CRM terrain for single wheel and full rover simulations. Specifically, the SCM and CRM DrawBar-Pull force and terrain slope vs. wheel slip curves match well, which indicates that the most likely set of parameters calibrated via the virtual bevameter and Bayesian framework leads to a predictive SCM model. When its use is granted, i.e., for simple wheel geometry, low to moderate shear, and low sinkage, SCM runs one order of magnitude faster than CRM. It is noted that when an actual bevameter testing rig can be used to produce experimental data, the Bayesian framework described herein continues to serve its calibration purpose. Ongoing work seeks to: (*i*) investigate how rover wheel grousers affect the accuracy of the SCM simulations; (*ii*) further validate the SCM method against experimental data. All simulations carried out in this contribution draw on scripts and models available in a public repository (Hu et al., 2022a) for reproducibility studies, as well as for unfettered use and distribution.

**Acknowledgments**

Support for this work was provided by National Science Foundation grants OAC2209791 and CMMI2153855, and US Army Research Office, under grants W911NF1910431 and W911NF1810476.

**References**

Andrieu, C., De Freitas, N., Doucet, A., and Jordan, M. I. (2003). An introduction to MCMC for machine learning. *Machine learning*, 50(1):5–43.

Apfelbeck, M., Kuß, S., Rebele, B., and Schäfer, B. (2011). A systematic approach to reliably characterize soils based on bevameter testing. *Journal of Terramechanics*, 48(5):360–371.

Bardenhagen, S., Brackbill, J., and Sulsky, D. (2000). The material point method for granular materials. *Computer methods in applied mechanics and engineering*, 187(3):529–541.

Baumgarten, A. S. and Kamrin, K. (2019). A general fluid–sediment mixture model and constitutive theory validated in many flow regimes. *Journal of Fluid Mechanics*, 861:721–764.

Bekker, M. G. (1956). *Theory of land locomotion; the mechanics of vehicle mobility*. University of Michigan Press, Ann Arbor.

Bui, H. H., Fukagawa, R., Sako, K., and Ohno, S. (2008). Lagrangian meshfree particles method (sph) for large deformation and failure flows of geomaterial using elastic–plastic soil constitutive model. *International Journal for Numerical and Analytical Methods in Geomechanics*, 32(12):1537–1570.

Chauchat, J. and Médale, M. (2014). A three-dimensional numerical model for dense granular flows based on the $\mu$(I) rheology. *Journal of Computational Physics*, 256:696–712.

Chen, J.-Y., Lien, F.-S., Peng, C., and Yee, E. (2020). Gpu-accelerated smoothed particle hydrodynamics modeling of granular flow. *Powder Technology*, 359:94–106.

Chen, W. and Qiu, T. (2012). Numerical simulations for large deformation of granular materials using smoothed particle hydrodynamics method. *Int. J. Geomechanics*, 12(2):127–135.

Chiang, H.-H., Wu, S.-J., Perng, J.-W., Wu, B.-F., and Lee, T.-T. (2010). The human-in-the-loop design approach to the longitudinal automation system for an intelligent vehicle. *IEEE Transactions on Systems, Man, and Cybernetics-Part A: Systems and Humans*, 40(4):708–720.

Cundall, P. A. and Strack, O. D. (1979). A discrete numerical model for granular assemblies. *Geotechnique*, 29(1):47–65.

DeDonato, M., Dimitrov, V., Du, R., Giovacchini, R., Knoedler, K., Long, X., Polido, F., Gennert, M. A., Padır, T., Feng, S., et al. (2015). Human-in-the-loop control of a humanoid robot for disaster response: a report from the darpa robotics challenge trials. *Journal of Field Robotics*, 32(2):275–292.

Dunatunga, S. and Kamrin, K. (2015). Continuum modelling and simulation of granular flows through their many phases. *Journal of Fluid Mechanics*, 779:483–513.

Edwards, M. B., Dewoolkar, M. M., Huston, D. R., and Creager, C. (2017). Bevameter testing on simulant fillite for planetary rover mobility applications. *Journal of Terramechanics*, 70:13–26.

Fatehi, R. and Manzari, M. T. (2011). Error estimation in smoothed particle hydrodynamics and a new scheme for second derivatives. *Computers & Mathematics with Applications*, 61(2):482–498.

Flegal, J. M., Haran, M., and Jones, G. L. (2008). Markov chain Monte Carlo: Can we trust the third significant figure? *Statistical Science*, 23(2):250 – 260.

Gelman, A., Carlin, J. B., Stern, H. S., and Rubin, D. B. (1995). *Bayesian data analysis*. Chapman and Hall/CRC.

Gingold, R. A. and Monaghan, J. J. (1977). Smoothed particle hydrodynamics-theory and application to non-spherical stars. *Monthly Notices of the Royal Astronomical Society*, 181(1):375–389.

Gray, J. P., Monaghan, J. J., and Swift, R. (2001). SPH elastic dynamics. *Computer methods in applied mechanics and engineering*, 190(49-50):6641–6662.

Hu, W., Guo, G., Hu, X., Negrut, D., Xu, Z., and Pan, W. (2019). A consistent spatially adaptive smoothed particle hydrodynamics method for fluid-structure interactions. *Comp. Meth. in Applied Mech. and Eng.*, 347:402–424.

Hu, W., Li, P., Serban, R., and Negrut, D. (2022a). Public Metadata: Calibration of an expeditious terramechanics model using a higher-fidelity model, Bayesian-inference, and a virtual bevameter test. `https://github.com/uwsbel/public-metadata/tree/master/2022/CRM2SCM_Paper/chrono_scripts`. Simulation-Based Engineering Laboratory, University of Wisconsin-Madison.

Hu, W., Rakhsha, M., Yang, L., Kamrin, K., and Negrut, D. (2021a). Modeling granular material dynamics and its two-way coupling with moving solid bodies using a continuum representation and the SPH method. *Computer Methods in Applied Mechanics and Engineering*, 385:114022.

Hu, W., Zhou, J., Serban, R., and Negrut, D. (2021b). Using an sph-based continuum representation of granular terrain to simulate the rover mobility. In *International Design Engineering Technical Conferences and Computers and Information in Engineering Conference*, volume 85468, page V009T09A028. American Society of Mechanical Engineers.

Hu, W., Zhou, Z., Chandler, S., Apostolopoulos, D., Kamrin, K., Serban, R., and Negrut, D. (2022b). Traction control design for off-road mobility using an SPH-DAE co-simulation framework. *Multibody System Dynamics*, 55:165–188.

Hurley, R. C. and Andrade, J. E. (2017). Continuum modeling of rate-dependent granular flows in SPH. *Computational Particle Mechanics*, 4(1):119–130.

Ionescu, I. R., Mangeney, A., Bouchut, F., and Roche, O. (2015). Viscoplastic modeling of granular column collapse with pressure-dependent rheology. *Journal of Non-Newtonian Fluid Mechanics*, 219:1–18.

Iwashita, K. and Oda, M. (1999). *Mechanics of Granular Materials: an Introduction*. CRC press.

Janosi, Z. and Hanamoto, B. (1961). The analytical determination of drawbar pull as a function of slip for tracked vehicles in deformable soils. In *Proc of the 1$^{st}$ int conf mech soil–vehicle systems. Turin, Italy*.

Jensen, R. P., Bosscher, P. J., Plesha, M. E., and Edil, T. B. (1999). DEM simulation of granular media—structure interface: effects of surface roughness and particle shape. *International journal for numerical and analytical methods in geomechanics*, 23(6):531–547.

Johnson, J. B., Kulchitsky, A. V., Duvoy, P., Iagnemma, K., Senatore, C., Arvidson, R. E., and Moore, J. (2015). Discrete element method simulations of Mars exploration rover wheel performance. *Journal of Terramechanics*, 62:31–40.

Krenn, R. and Gibbesch, A. (2011). Soft soil contact modeling technique for multi-body system simulation. In *Trends in computational contact mechanics*, pages 135–155. Springer.

Krenn, R. and Hirzinger, G. (2009). SCM – a soil contact model for multi-body system simulations. In *11th European Regional Conference of the International Society for Terrain-Vehicle Systems - ISTVS 2009*.

Kumar, R., Carroll, C., Hartikainen, A., and Martin, O. (2019). ArviZ: a unified library for exploratory analysis of Bayesian models in Python. *Journal of Open Source Software*, 4(33):1143.

Lucy, L. B. (1977). A numerical approach to the testing of the fission hypothesis. *The Astronomical Journal*, 82:1013–1024.

Mason, G. L., Salmon, J. E., McLeod, S., Jayakumar, P., Cole, M. P., and Smith, W. (2020). An overview of methods to convert cone index to bevameter parameters. *Journal of Terramechanics*, 87:1–9.

Meirion-Griffith, G. and Spenko, M. (2011). A modified pressure–sinkage model for small, rigid wheels on deformable terrains. *Journal of Terramechanics*, 48(2):149–155.

Monaghan, J. J. (2000). SPH without a tensile instability. *Journal of Computational Physics*, 159(2):290–311.

Monaghan, J. J. (2005). Smoothed Particle Hydrodynamics. *Reports on Progress in Physics*, 68(1):1703–1759.

Negrut, D. and Mazhar, H. (2017). Sand to mud to fording: Modeling and simulation for off-road ground vehicle mobility analysis. In *International Workshop on Bifurcation and Degradation in Geomaterials*, pages 235–247. Springer.

Nguyen, C. T., Nguyen, C. T., Bui, H. H., Nguyen, G. D., and Fukagawa, R. (2017). A new SPH-based approach to simulation of granular flows using viscous damping and stress regularisation. *Landslides*, 14(1):69–81.

Recuero, A. M., Serban, R., Peterson, B., Sugiyama, H., Jayakumar, P., and Negrut, D. (2017). A high-fidelity approach for vehicle mobility simulation: Nonlinear finite element tires operating on granular material. *Journal of Terramechanics*, 72:39 – 54.

Robert, C. P. (2015). The metropolis-hastings algorithm.

Salvatier, J., Wiecki, T. V., and Fonnesbeck, C. (2016). Probabilistic programming in Python using PyMC3. *PeerJ Computer Science*, 2:e55.

Serban, R., Taves, J., and Zhou, Z. (2022). Real time simulation of ground vehicles on deformable terrain. In *Proceedings of ASME IDETC/CIE 2022*, St. Louis, MO.

Smith, W., Melanz, D., Senatore, C., Iagnemma, K., and Peng, H. (2014). Comparison of discrete element method and traditional modeling methods for steady-state wheel-terrain interaction of small vehicles. *Journal of Terramechanics*, 56:61–75.

Soga, K., Alonso, E., Yerro, A., Kumar, K., and Bandara, S. (2016). Trends in large-deformation analysis of landslide mass movements with particular emphasis on the material point method. *Géotechnique*, 66(3):248–273.

Sulsky, D., Chen, Z., and Schreyer, H. L. (1994). A particle method for history-dependent materials. *Computer methods in applied mechanics and engineering*, 118(1-2):179–196.

Tasora, A., Mangoni, D., Negrut, D., Serban, R., and Jayakumar, P. (2019). Deformable soil with adaptive level of detail for tracked and wheeled vehicles. *International Journal of Vehicle Performance*, 5(1):60–76.

Tasora, A., Serban, R., Mazhar, H., Pazouki, A., Melanz, D., Fleischmann, J., Taylor, M., Sugiyama, H., and Negrut, D. (2016). Chrono: An open source multi-physics dynamics engine. In Kozubek, T., editor, *High Performance Computing in Science and Engineering – Lecture Notes in Computer Science*, pages 19–49. Springer International Publishing.

Ucgul, M., Fielke, J., and Saunders, C. (2015). Three-dimensional discrete element modeling (DEM) of tillage: Accounting for soil cohesion and adhesion. *Biosystems Engineering*, 129:298–306.

Vehtari, A., Gelman, A., Simpson, D., Carpenter, B., and Bürkner, P.-C. (2021). Rank-normalization, folding, and localization: An improved $\hat{R}$ for assessing convergence of MCMC (with discussion). *Bayesian Analysis*, 16(2).

Wong, J. Y. (2001). *Theory of Ground Vehicles*. John Wiley & Sons, New York.

Xu, W.-J., Dong, X.-Y., and Ding, W.-T. (2019). Analysis of fluid-particle interaction in granular materials using coupled sph-dem method. *Powder Technology*, 353:459–472.

Yue, Y., Smith, B., Batty, C., Zheng, C., and Grinspun, E. (2015). Continuum foam: A material point method for shear-dependent flows. *ACM Transactions on Graphics (TOG)*, 34(5):1–20.

Zhao, C.-L. and Zang, M.-Y. (2017). Application of the FEM/DEM and alternately moving road method to the simulation of tire-sand interactions. *Journal of Terramechanics*, 72:27–38.